

A Tunable Nanoplasmonic Mirror at an Electrochemical Interface

Ye Ma,[†] Cristian Zagar,[†] Daniel J. Klemme,[‡] Debabrata Sikdar,^{†,§} Leonora Velleman,[†] Yunuen Montelongo,[†] Sang-Hyun Oh,[‡] Anthony R. Kucernak,^{*,†,§} Joshua B. Edel,^{*,†,§} and Alexei A. Kornyshev^{*,†,§}

[†]Department of Chemistry, Imperial College London, London, SW7 2AZ, United Kingdom

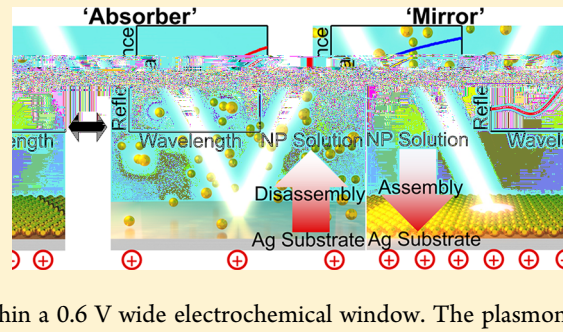
[‡]Department of Electrical and Computer Engineering, University of Minnesota, Minneapolis, Minnesota 55455, United States

[§]Department of Electronics and Electrical Engineering, Indian Institute of Technology Guwahati, Guwahati-781039, India

Supporting Information

ABSTRACT: Designing tunable optical metamaterials is one of the great challenges in photonics. Strategies for reversible tuning of nanoengineered devices are currently being sought through electromagnetic or piezo effects. For example, bottom-up self-assembly of nanoparticles at solid | liquid or liquid | liquid interfaces can be used to tune optical responses by varying their structure either chemically or through applied voltage. Here, we report on a fully reversible tunable-color mirror based on a TiN-coated Ag substrate immersed in an aqueous solution of negatively charged Au-nanoparticles (NPs). Switching electrode potential can be used to fully control the assembly/disassembly of NPs at the electrode | electrolyte interface within a 0.6 V wide electrochemical window. The plasmon coupling between the electrode and the adsorbed NP array at high positive potentials produces a dip in the optical reflectance spectrum, creating the “absorber” state. Desorption of NPs at low potentials eliminates the dip, returning the system to the reflective “mirror” state. The intensity and wavelength of the dip can be finely tuned through electrode-potential and electrolyte concentration. The excellent match between the experimental data and the theory of optical response for such system allows us to extract valuable information on equilibrium and kinetic properties of NP-assembly/disassembly. Together with modeling of the latter, this study promotes optimization of such meta-surfaces for building electrotunable reflector devices.

KEYWORDS: *metamaterials, nanoparticle self-assembly, electrochemical interface, realtime tunability, plasmonics, electrosorption*



Metamaterials based on periodic subwavelength structures possess exceptional optical properties for manipulating light-matter interactions.^{1–5} For instance, invisibility cloaks,^{6,7} super lenses,^{8–10} color display,^{11,12} and nanoantenna for solar energy^{13–16} have demonstrated the “programmable” nature of metamaterials with numerous promising applications.^{17–19} The most extensively studied ones have been the strongly coupled plasmonic systems exhibiting exotic dielectric and magnetic properties.^{20–22}

There is currently a strong demand for *in situ* tunability of the optical properties of such systems.^{19,21,23,24} For normally static architectures built by conventional lithography,¹ mechanical^{24–26} and thermal²⁷ effects that induce physical deformation of the materials are already widely used to tune the output without need for major reconstruction of the topology. Alternatively, bottom-up methods, based on self-assembly of nanoscale building blocks, can be used for *in situ* generation of structures and the tailoring of their spectral response.^{28–37}

Systems composed of nanoparticles (NPs) deposited on metallic substrates (NPoMS), where NPs and substrates are electromagnetically coupled, have been shown to be tailororable by varying the component materials, shape, size, and spacing between the NPs and between the NPs and the substrate.^{38–42}

Such systems have been widely exploited in sensing^{43,44} optical nonlinearity,⁴⁵ nanoantennas,⁴⁶ and surface-enhanced Raman spectroscopy (SERS).⁴⁷ However, one of the most challenging tasks is to be able to reversibly change the structure and tailor the properties of these systems in real-time.^{23,48,49}

Several steps have been taken in this direction, including structures wherein an aluminum substrate was coupled to gold NPs.⁵⁰ Aluminum being naturally reactive, the light scattering from such an interface was continuously tuned through the oxidation of aluminum. An alternative is to tether NPs on metallic substrates in a liquid environment. For tethered cuboid NPs on transparent electrodes, theory has estimated that the reflection spectrum can be visibly affected by the orientation of the cuboids when a voltage is applied to the electrode.⁵¹ Earlier, Mock et al. have successfully anchored gold NPs onto a gold substrate through the linkage of a charged polymer interlayer.⁵² By applying different electrode potentials on the gold substrates, reversible tuning of local plasmonic coupling was achieved. Furthermore, Di Martino et al. have shown a continuous adjustment of SERS spectra upon

Received: August 7, 2018

Published: October 25, 2018



ACS Publications

© 2018 American Chemical Society

4604

DOI: 10.1021/acspolymers.8b01105
ACS Photonics 2018, 5, 4604–4613

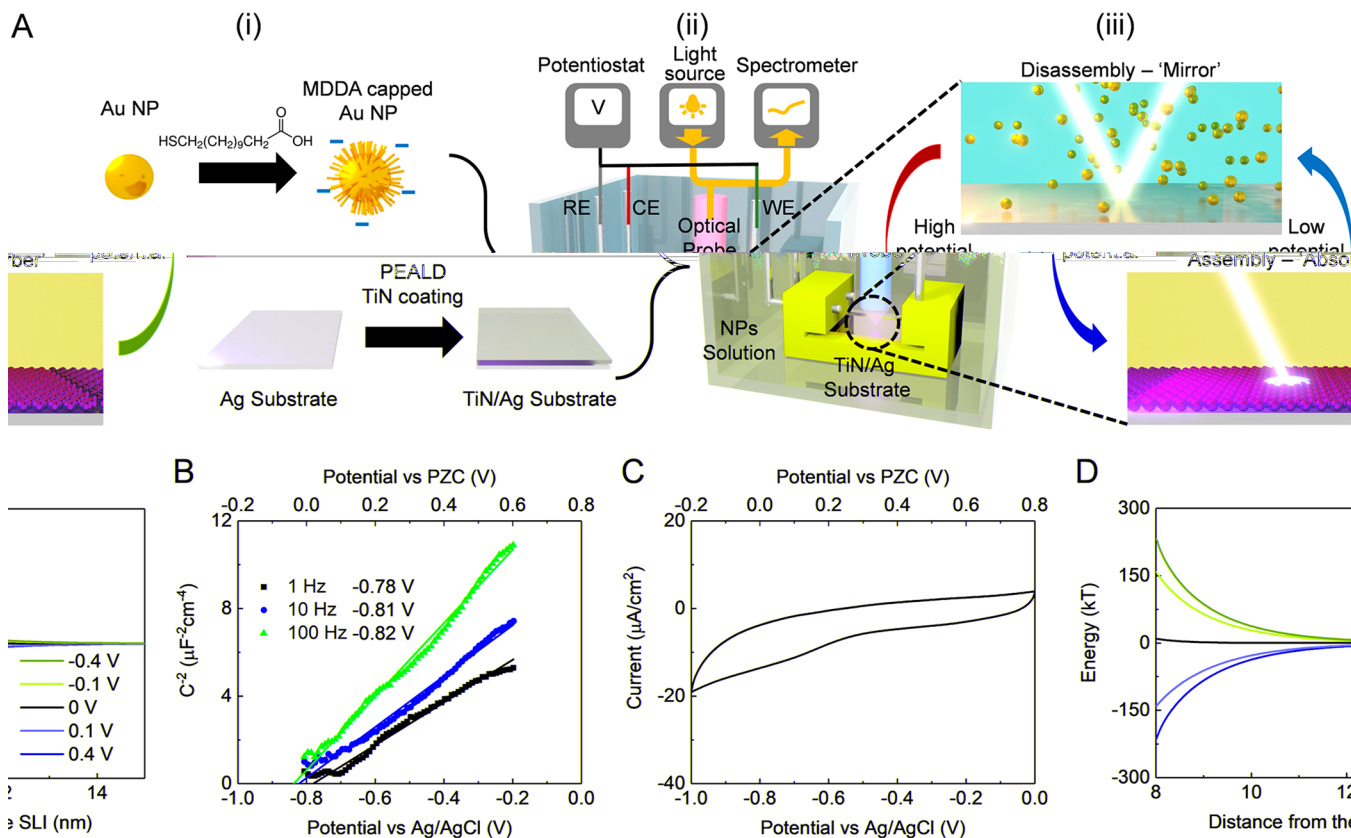


Figure 1. Principles of electro-switchable “mirror”/“absorber”. (A) Experimental scheme: (i) Functionalization of Au NPs and coating of the silver substrate. (ii) Three-electrode electrochemical-optical cell, including TiN/Ag substrate (in a PTFE holder) as the working electrode, Ag/AgCl and Pt serving as reference and counter electrodes, respectively, and the optical probe focused vertically on the substrate to collect the reflectance signal at normal incidence. (iii) Switching between “absorber” and “mirror” states via assembling or disassembling NPs on TiN/Ag. (B) Mott–Schottky plot for the capacitance of TiN/Ag electrode in 60 mM NaCl aqueous solution, determining PZC under 1, 10, and 100 Hz impedance measurements. (C) Cyclic voltammogram of TiN/Ag in 60 mM NaCl with 20 mV/s scanning rate. (D) Typical model calculation of the electrostatic self-energy profiles of individual NPs as a function of distance to the working electrode at different applied potentials (vs PZC) for such solution: it demonstrates a crossover from attraction to repulsion at large enough negative potentials of the electrode.

variation of potential using a gold electrode coated with a self-assembled monolayer (SAM) of thiolated molecules onto which gold NPs were placed.⁵³ However, the optical tunability is limited since the NPs are attached to the substrate.

Recently, we reported on the creation of an electrotunable nanoplasmonic liquid mirror based on NP assembly at an interface of two immiscible electrolytic solutions (ITIES).⁵⁴ Within the potential window at which ions do not cross the interface, oppositely charged electrical double layers form on both sides of the liquid | liquid interface (LLI). When the aqueous phase is polarized negatively relative to the organic phase, the energy well for negatively charged NPs at the interface deepens, facilitating the formation of a dense arrays of NPs at the interface. This array provides substantial reflection of the incident light. On the other hand, polarizing the aqueous phase positively destroys the well, pushing NPs back to the aqueous bulk, switching off the nanoplasmonic liquid mirror.

In the present paper we show that voltage-controlled assembly/disassembly of NP arrays can be achieved also at a “classical” electrochemical electrode | electrolyte interfaces. But the effect of this manipulation is entirely different from the ITIES case. In the NPMS system under study, we show that by changing electrode potential we can reversibly tune the outputs between “absorber” and “mirror” states.

The coupling between dissipating localized plasmons of adsorbed gold NPs and surface plasmons on the metallic electrode contributes to absorption of incident light.⁵⁵ The absorption intensity, the wavelength at its maximum, and to a lesser extent, the breadth of the absorption band, all depend on the size of NPs and the density of NP arrays. For a given size of NP, this absorption causes a dip in the reflectance spectrum. It deepens with densification of the NP array, and the wavelength of the reflection minimum moves toward the red. The state with the quenched reflection will hereafter be called the “absorber” state, as compared to the “mirror” state of the bare substrate.

Specifically, the switchable device that we present below is based on a silver electrode covered with a thin protective TiN film, accommodated in an electrochemical cell composed of aqueous NaCl electrolyte and dispersed gold NPs. Due to a large negative charge on the NPs, an energy well trapping NPs at the interface is formed when the TiN/Ag substrate is positively polarized. With careful control of the NaCl concentration, which provides screening of electrostatic interactions, the average distance between the neighboring NPs and, thereby, the overall density of the array of NPs on the TiN/Ag surface can be tuned. To switch the device from the “absorber” back to its “mirror” state, we need to reduce the positive potential of the TiN/Ag electrode. This will make the

energy well for NPs at the solid–liquid interface (SLI) shallower or even completely eliminated, thus, facilitating desorption of NPs. This process is fully reversible within a 0.6 V wide electrochemical window.

The coverage of NPs on the electrode can be estimated through comparing the variation of experimentally measured reflectance spectra with theoretical ones, in which the main input parameter is the average distance between the assembled NPs.⁵⁶

As compared with previous systems, where dried or tethered NPs on metallic substrates were used, ours has numerous advantages: (i) it is based on controlled self-assembly of NPs; (ii) real-time tailoring of interparticle distances can tune the reflectance spectrum, including the reversible turning on-and-off of the “absorber”/“mirror” states; (iii) the homogeneous distribution of electric field on the planar electrode substrate provides a convenient up-scaling route for macroscale applications.

■ EXPERIMENTAL SYSTEM AND THEORETICAL FRAMEWORK

Electrochemical-Optical Cell. The substrate for the solid–liquid interface was made from 10.0 ± 0.2 nm thick TiN deposited via atomic layer deposition on 125 nm thick Ag on silicon, Figure 1A(i). Ag surfaces are ideal reflectors of visible light, widely used in a variety of optical applications. However, when in contact with aqueous environments, Ag is vulnerable to oxidation. A thin film of TiN was therefore deposited on top of the Ag surface to minimize corrosion. Importantly, this TiN film is thin enough to provide good transparency and electronic conduction.^{57–59} The TiN/Ag substrate was interfaced into an electrochemical cell and used as the working electrode, Figure 1A(ii). The cell also accommodated a reference and a counter electrode, along with a vertically aligned fiber coupled optical probe for focusing and collecting light.

By biasing the working electrode, it was possible to reversibly control assembly and disassembly of 16 ± 1 nm gold NPs, introduced in the aqueous phase, to and from the TiN/Ag substrate. This has the net effect of switching the device between “absorber” and “mirror” states, Figure 1A(iii). The as-made citrate-capped NPs are prone to aggregation at high ionic strengths.⁶⁰ To minimize aggregation, the ligand was exchanged with 12-mercaptopododecanoic acid (MDDA) which has been shown to stabilize NPs in a wide range of salt concentrations (detailed NP stability tests can be found in SI, section 2).⁵⁴ These molecules possess high affinity⁶¹ to the gold surface of the NPs and its carboxylic acid moieties ($pK_a = 4.8$) is dissociated at the experimental pH = 6.2, leaving negative charges on the terminal groups (for details, see SI, section 3). The negatively charged MDDA furthermore facilitates voltage-control of the assembly and disassembly process.

Potential of Zero Charge and Electrochemical Window. To understand and control the assembly and disassembly of NPs by changing electrode potential, it is important to delineate the electrode potential with respect to the potential of zero charge (PZC). Measurements of interfacial capacitance may help to evaluate the latter. The capacitance of the TiN/Ag substrates was measured using 60 mM NaCl at frequencies of 1, 10, and 100 Hz, as shown in Figure 1B. For its interpretation, the following considerations should be kept in mind.

Without a significant electrical current across the electrode | electrolyte interface, TiN is believed to behave like an n-type semiconductor⁶² capable of forming a space-charge⁶³ at the SLI alongside the counter-charge of the ionic double layer. This adds space charge capacitance, C_{sc} , in series to the double layer capacitance, C_{dl} . Therefore, the total capacitance of the interface is $C = (C_{sc}^{-1} + C_{dl}^{-1})^{-1}$. The smaller of the two capacitances will therefore dominate it and, in our case, is seemingly the space-charge one.

Indeed, the double layer capacitance in aqueous electrolytes of the type we used close to PZC is about $15\text{--}18 \mu\text{F}/\text{cm}^2$, whereas the values of C that we observe are close to $1 \mu\text{F}/\text{cm}^2$.⁶⁴ Furthermore, the voltage dependence of C^{-2} shown in Figure 1B increases rather than decreases with electrode potential as would have been for the case for double layer Gouy–Chapman capacitance.⁶⁴ The measured capacitance rather obeys the Mott–Schottky law⁶⁵ for a semiconductor, $C_{sc}^{-2} \propto E - E_{PZC} - k_B T/e$, where E is the applied potential, E_{PZC} is the potential of zero charge, k_B is the Boltzmann constant, and T the absolute temperature ($k_B T/e$ is the so-called thermal voltage, at room temperature = 0.0256 V). Figure 1B displays a linear-like relationship between the potential and C^{-2} , which suggests that the space charge capacitance dominates the overall interfacial capacitance. This agrees with literature for similar systems.^{62,66,67} For all three frequencies, the plots consistently returned the same intercept at -0.8 V versus Ag/AgCl, which acts as a good estimate for the PZC. This value of PZC will be taken as the prime reference when we are discussing potentials applied to the substrates.

Cyclic voltammetry with NPs present was performed to determine the electrochemical window of the system (Figure 1C) over which range no unwanted electrochemical reactions take place. The potential window was therefore determined to be 0.1 to 0.7 V vs PZC (-0.7 to -0.1 V vs reference electrode). In this range, the maximum current density does not exceed $15 \mu\text{A}/\text{cm}^2$ at a scan rate of 20 mV/s. The amount of charge during one assembly and one disassembly processes are 1.2 mC cm^{-2} (i.e., an average current of $0.2 \mu\text{A cm}^{-2}$) and -11 mC cm^{-2} (an average current of $-1.8 \mu\text{A cm}^{-2}$). We attribute this asymmetrical charge transfer to the low operation potential (-0.7 V vs Ag/AgCl) during the disassembly process leading to the occurrence of oxygen reduction. For future compact devices, a sealed cell from the atmosphere would possibly lower this current. The low average current and relatively high electrolyte concentration suggest that any ohmic potential drop is $\ll 1$ mV; therefore, electrophoretic effects may be ignored. Although a more positive electrode bias may favor even denser NP assembly, potentials above 0.7 V versus PZC were not used, as it would lead to oxidation of the silver substrate even through the TiN coating.

Optical Reflectivity. A “five-layer” effective-medium theory (EMT) was used to interpret the optical reflectance spectra, the foundations of which were presented in ref 55. For a given lateral structure of the NP array, its contribution to the system optical response, in this theory, can be described as that of a pseudofilm. The frequency-dependent dielectric polarizability of that “film” is expressed through the optical polarizability of individual NPs which is described within a dipolar approximation. The theory accounts for interactions of localized plasmons in NPs: with each other, with the substrate, and the surrounding medium. Once the dielectric polarizability of such film is calculated, it is imbedded into the Fresnel’s

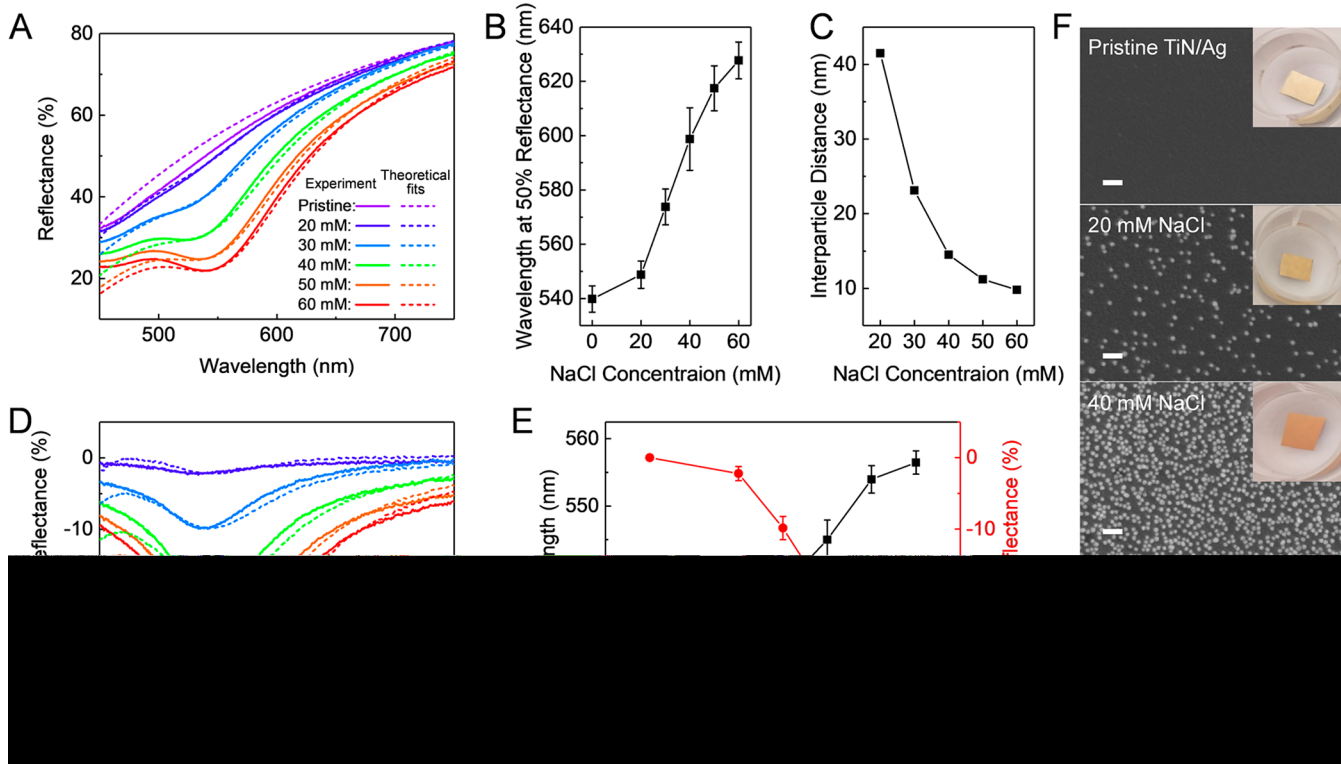


Figure 2. Controlling the assembly of NPs on TiN/Ag by varying NaCl concentrations at an applied potential of 0.7 V vs PZC. (A) Experimental (solid) and theoretically fitted (dashed) reflectance curves of NPs assembly on TiN/Ag at different concentrations of NaCl after 12 h deposition of NPs at 0.7 V vs PZC. The wavelengths at 50% reflectance (B) and the evaluated interparticle distances (C) for NPs assembled on TiN/Ag at different concentrations of NaCl. (D) Experimental (solid) and theoretically fitted (dashed) curves of the change in reflectance of NPs/TiN/Ag for different NaCl concentrations, with respect to the pristine TiN/Ag substrate, which shows the broad reflectance dip evolving with densification of the adsorbed NP array. (E) Derived from Panel D, the wavelength (black squares) and the change of reflectance (red dots) of the dip. (F) SEM of dried samples after NP assembling under indicated electrolyte conditions; scale bar 100 nm; the white dots represent the adsorbed NPs, shown at the dark background of bare TiN/Ag substrate. Digital camera photos (insets) of wet samples after NP assembling on TiN/Ag under indicated electrolyte conditions. Note, the spectra obtained at 0 mM NaCl are not shown in A and D, but were still treated in the same way as the other concentrations.

theory of the multilayered system. In our case, the five-layer stack comprises aqueous electrolyte, NP layer, spacer, TiN film, and a semi-infinite Ag electrode. The details of the theory and basic equations for the calculation of the reflectivity signals are presented in the Methods and SI, section 4. Assuming that NPs adsorb at the interface but electrostatically repel each other and thereby form a hexagonal array,³⁵ the calculated reflection spectra will only depend on the average spacing between NPs. Although experimentally the interparticle distance will have dispersion, a brief examination about its deviation (SI, section 5 and Figure S6) shows that the reflectance is not very sensitive to deviations from a uniform particle distribution.

Thus, calculated reflection spectra can be fitted to the experimental reflectivity spectra, giving the array density. We will first apply this procedure to the equilibrium data obtained at different applied voltages. We further apply it to study the kinetics of adsorption–desorption, by monitoring the dynamics of change of reflection spectra, after abrupt change of the electrode potential. This will give us full information about the voltage-controlled assembly disassembly of NP arrays. The comparison of the measured and thus calculated reflectance spectra will let us test the validity of the overall picture, and identify the key effects that govern the assembly process.

Adsorption equilibria. Assembly of NPs at an SLI requires the balancing of forces, between NPs and the

interface, and between NPs themselves. The main forces acting between NPs, both in the bulk and on the surface, are van der Waals attraction and electrostatic repulsion. Electrostatic forces need to be strong enough to stop NPs from coming too close to each other, otherwise van der Waals interactions may force the NPs to aggregate. As described in the previous sections and SI, section 2, to make the solution stable, these forces are carefully adjusted by the pH and electrolyte concentration, thereby tuning, respectively, the average charge of NPs and the screening of electrostatic interactions. The variation of electrolyte concentration not only NP stability in the bulk solution, but also affects the interparticle forces at the interface.⁶⁸

The interaction of NPs with the substrate include image interactions of charged NPs with the interface, image-modified pair interaction between NPs at the interface, and the corresponding van der Waals interactions.

Electrostatic interactions of this kind are complicated by the strong nonlinear response of electrolyte to charged NPs. Nevertheless, we perform calculations within the linear response approximation, to get a flavor of the balance of forces that allows particles to adsorb at high positive electrode potentials and desorb at low ones, respectively.

Careful analysis has shown that van der Waals forces for the system we are studying here are less important than electrostatic interactions. We, therefore, rest our conclusions

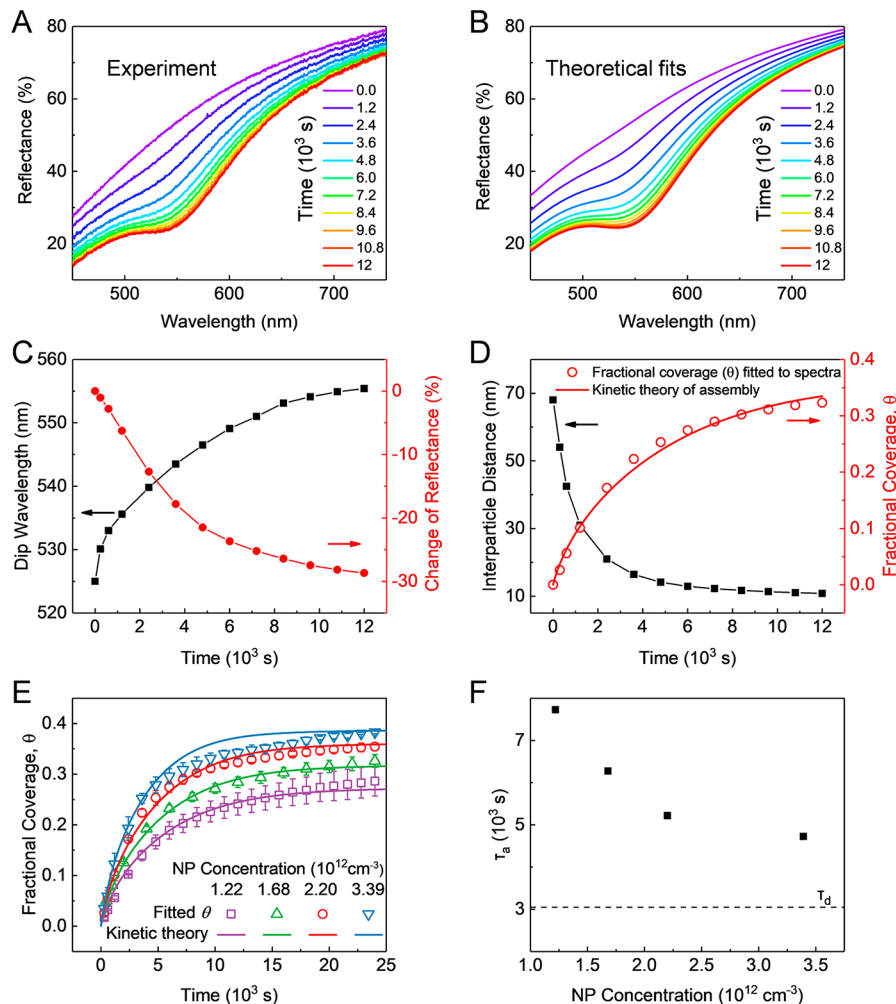


Figure 3. Kinetics of the NP assembly triggered by electrode potential. Experimental (A) and theoretically fitted (B) time-dependent reflectance curves of NPs assembled on TiN/Ag in a solution of $2.2 \times 10^{12} \text{ cm}^{-3}$ NPs and 60 mM NaCl under 0.7 V vs PZC, starting from pristine TiN/Ag. (C) Corresponding experimental time-dependent wavelengths (black squares) and the change of reflectance (red dots) at the reflection dip (obtained by subtracting the reflectance data for pristine TiN/Ag from Panel A). (D) Time-dependent interparticle distances (black squares); the fractional coverage $\theta(t)$ (red empty circles), as extracted from fitting the theory to reflectance data, and the numerical results from the kinetic adsorption theory (red line), as described in the text. (E) The extracted fractional coverage $\theta(t)$ (empty symbols) and the results of kinetic adsorption theory (lines) corresponding to the indicated concentrations of NPs. (F) Fitted characteristic “adsorption time” (τ_a) and “desorption time” (τ_d) involved in the kinetic adsorption theory (see the text) for different concentrations of NPs.

on feasibility of the voltage-controlled adsorption–desorption predominantly on electrostatic calculations (for details, see *Methods*). Figure 1D shows typical results of such calculations for the described system: the computed, interaction energy of one NP with the electrode as a function of a distance from its surface. One can clearly see that this interaction can be easily switched between attractive and repulsive modes, indicating the possibility of tuning the system by varying the electrode potential.

Adsorption Kinetics. To describe the kinetics of NP adsorption–desorption, monitored through fitting the measured and calculated reflectance data, we adopt a phenomenological theory developed in colloid and interface science.⁶⁹ That theory accounts for all three stages of the process, describing the balance between the diffusion to the interface and the surface adsorption and desorption rates; an overview of its key principles and equations used is given in the *Methods*.

RESULTS AND DISCUSSION

Assembly of NPs: the “Absorber” State. As discussed above (Figure 1D), at high positive potential versus PZC, NPs are expected to be trapped within the energy well at the SLI to form a two-dimensional plasmonic array. Although we do not have direct *in situ* structural information about such NP arrays,³⁵ we can extract an average distance between NPs from the measured reflection spectra, by comparing them with theory.

As seen in the static reflectance spectra (Figure 2A), the concentration of NaCl plays a vital role during the assembly process. The violet curve in Figure 2A shows the reflectance spectrum at normal incidence to the pristine TiN/Ag substrate when the device is in its “mirror” state. To assemble NPs on the substrate, that is, to switch the device to its “absorber” state, we polarize the substrate at 0.7 V vs PZC for 12 h to ensure equilibrium has been reached as after 3–4 h the optical signal remains almost constant. When the concentration of NaCl in the solution is less than 20 mM, the optical signal

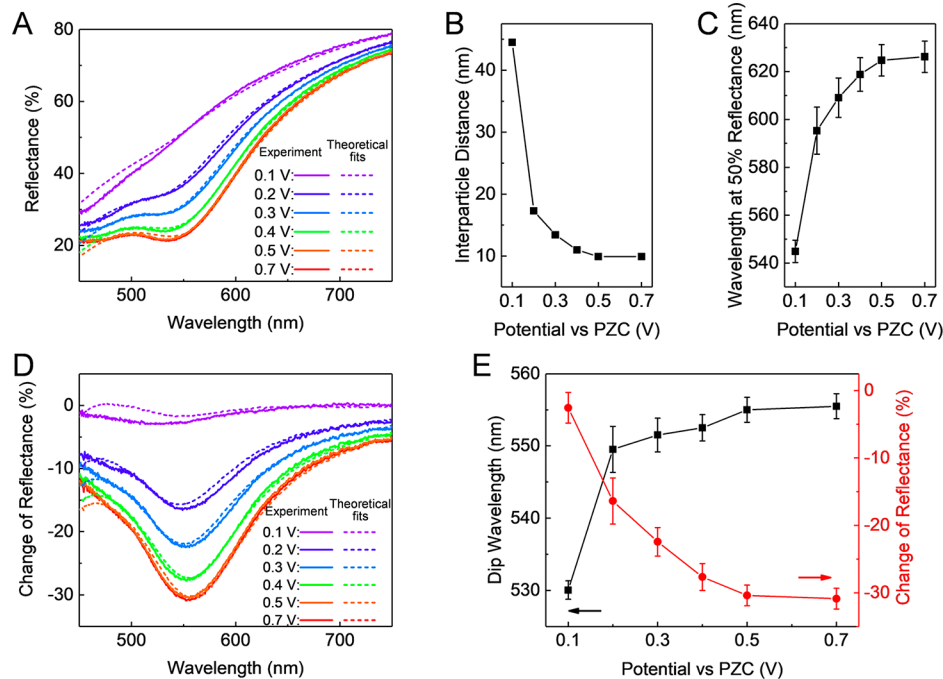


Figure 4. Disassembly of NPs on TiN/Ag, controlled by reducing the potential from the assembly potential (0.7 V vs PZC). (A) Experimental (solid) and theoretically fitted (dashed) reflectance curves of disassembling NPs on TiN/Ag in 60 mM NaCl under 0.1–0.7 V vs PZC. The experiments start from fully assembled NPs/TiN/Ag at 0.7 V vs PZC, with gradual disassembly by stepwise reducing the potential to 0.1 V vs PZC. The wavelength at 50% reflectance (B) and the fitted interparticle distances (C) for NPs assembled on TiN/Ag at different potentials (as derived from data in Panel A). (D) Experimental (solid) and theoretically fitted (dashed) curves of the change of reflectance of NP/TiN/Ag with respect to the pristine TiN/Ag substrate under different indicated potentials. (E) The wavelengths (black squares) and the change of reflectance (red dots) at the reflection dip, as derived from the data of Panel D.

remains predominantly unchanged due to the sparsely distributed NPs on the substrate. With the increase of the NaCl concentration, a concavity (dip) in reflectance spectra evolves within the visible range and the whole spectrum shifts to the red, Figure 2A. Specifically, the wavelength corresponding to 50% reflectance shifts from 540 to 628 nm when the concentration of NaCl increases to 60 mM, Figure 2B. This is caused by an increase in the number of adsorbed NPs at the interface as can clearly be seen via comparison with EMT. Fitting the theory to experimental data shows an excellent match between the two sets of curves and could therefore be used to determine the only fitting parameter—interparticle distance, Figure 2C. This absorption-induced concavity in the reflectance spectra evolving with assembly of NPs can be even better seen if the reflectance spectrum of the pristine substrate is subtracted from the spectra with adsorbed NPs (Figure 2D): Both the wavelength and the intensity of this dip increase with increasing NaCl concentration from zero up to 60 mM, giving rise to a wavelength shift from 525 to 557 nm and a maximal 30% drop in reflectance versus pristine silver mirror, Figure 2E.

Ex situ scanning electron microscopy (SEM) is a powerful tool to directly visualize the arrays formed at interfaces, albeit after drying. SEM images of rapidly dried samples shown in Figure 2F gives a glimpse of the effect of electrolyte concentration on NP density. Although array rearrangement during and after drying is likely, these images show similar trends in coverage to that discussed above. Namely, higher NaCl concentrations in the original solution results in increased NP densities on the substrate. The excellent agreement between the surface coverage estimates made from SEM image analysis and EMT reinforces the close

correlation between the experiments and our theoretical analyses, Figure S10.

The inset optical images in Figure 2F show the macroscale appearance of wet samples with NPs assembled on the substrates. The pristine substrate is the most reflective sample and appears golden due to the TiN-coating. The colors change from yellow to orange and then to red as the NP density is increased. These color changes are also consistent with our reflectance spectra: since the coupled substrate–NP system exhibit the reflectance dip centered around the green region.

The essential role of NaCl can be understood from theoretical modeling of the NP–NP pair interaction. The magnitudes of these interaction energies are plotted (Figure S3) against NP separations for multiple electrolyte concentrations. Electrostatic screening of repulsive interparticle forces can, therefore, be tuned by controlling the NaCl concentration, weakening repulsion to such a degree that NPs can assemble into a relatively dense array, giving rise to a strong change in reflectance. For details of the calculation of pair interactions see Methods.

To understand the dynamics of the assembly process, we monitored the reflectance over the course of the whole process. Figure 3A,B demonstrates the evolution of the experimental and theoretically fitted reflectance spectra for an immersed pristine TiN/Ag substrate in 60 mM NaCl NP solution at 0.7 V versus PZC. Fitting the theoretical reflectance spectra to the experimental ones, we extracted the interparticle distance and surface coverage at different time points (the conversion between the lattice constant and surface coverage is straightforward; the one for hexagonal lattice is exemplified in SI, section 5). Interpretation of results implies that the

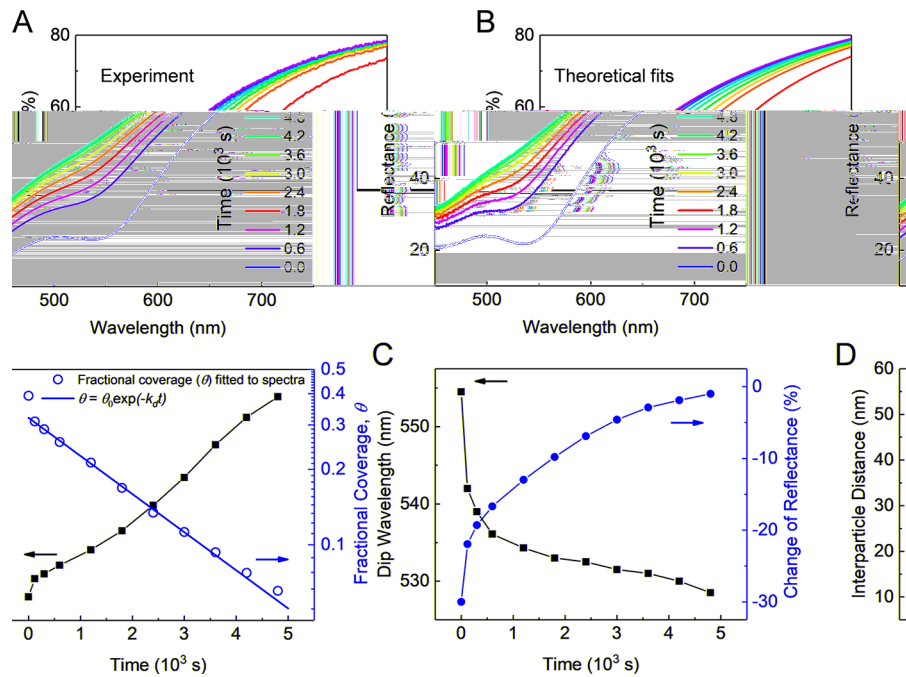


Figure 5. Desorption-limited kinetics of NP disassembly at 0.1 V vs PZC. Experimental (A) and theoretically fitted (B) time-dependent reflectance curves of NPs disassembling from TiN/Ag in a solution of $2.20 \times 10^{12} \text{ cm}^{-3}$ NP and 60 mM NaCl after an electrode potential jump from 0.7 to 0.1 V vs PZC, starting from fully assembled NPs/TiN/Ag. (C) The time-dependence of the wavelength (black squares) and of the change of reflectance (red dots) at the reflection dip obtained by subtracting the reflectance of pristine TiN/Ag. (D) Calculated time-dependent interparticle distances (black squares), fractional coverage $\theta(t)$ extracted from Panel B (red empty circles) and the exponential desorption isotherm [$\theta = \theta_0 \exp(-k_d t)$] (red straight line).

rearrangement of the lattice of adsorbed NPs is significantly faster than their diffusion toward the surface.

The depth of the reflection dip initially keeps deepening, asymptotically approaching a plateau around -30% (Figure 3C). At the same time, the wavelength of the dip red-shifts from 525 to 555 nm, which is consistent with our static data.

Interparticle distance/surface coverage (Figure 3D), calculated from fitting the reflectance data to the EMT theory (Figure 3B), helps to understand the dynamics of NP assembly at the SLI. By definition, surface coverage refers to the number of nanoparticles per unit area, while fractional coverage stands for the fraction of maximum coverage, Γ_m . The relationship between fractional coverage and reflectance is established based on the theoretical model for reflectance spectra, detailed in Methods and the SI, section 4. Figure 3D shows how interparticle distance decreases and fractional coverage, θ , increases after jump-wise imposing 0.7 V versus PZC. Coverage data are further found to have a good match with a kinetic model⁶⁹ (red line, also reviewed in Methods), which takes into account the contributions from adsorption, desorption, and diffusion. The fact that diffusion does not dominate the assembly process, at least initially (Figure S8, at the beginning, the coverage does not grow with time square-root-wise), indicates the presence of a free energy barrier that NPs have to overcome in order to reach the adsorption well.

The time evolution of the coverage obtained for four different concentrations of NPs is shown in Figure 3E. Fitting of the kinetic model allows us to evaluate characteristic adsorption and desorption times, τ_a and τ_d , the parameters of the kinetic adsorption isotherm, as described in Methods. The results are shown in Figure 3F, with τ_a as expected decreasing with the concentration of NPs. But their dependence is nontrivial. Generally, the rate constants, k_a and k_d of the

elementary acts of adsorption and desorption, are related to these times as $\tau_a^{-1} = k_a c_a$, where c_a is the concentration of NPs at the surface just before the adsorption barrier and $\tau_d^{-1} = k_d$. Increase of the bulk concentration of NPs could increase, proportionally, c_a at low concentrations, but such proportionality may no longer hold at higher concentrations. We see this from Figure S9. It might be, however, premature to speculate about this deviation because of the lower accuracy of the reflection signal at high NP concentration due to increased optical absorbance in the bulk, a potential reason for the less than good fit for the blue curve in Figure 3E.

Disassembly of NPs: the “Mirror” State. Upon assembly, in the “absorber” state, NPs are trapped in the energy wells at the SLI. To drive them away from the substrate and switch back to a “mirror”, one must lower the electrode potential, making it less positive with respect to the PZC, which is expected to weaken the adsorption well and, correspondingly, diminish the barrier that hinders the escape of NPs from the well. This is confirmed from the trend seen when we lower the potential of the NPs/TiN/Ag. Figure 4A shows the static reflectance spectra at different electrode potentials. At high potentials (0.5–0.7 V), the NPs will not be released from the SLI back into the bulk solution, and data from EMT fitting indicates that the interparticle distance remains almost unchanged, Figure 4B. This suggests that the energy well at the SLI is still substantial. By further lowering the potential, a dramatic weakening of the optical signal is observed and accompanied by a substantial blue shift of the wavelength of 50% reflectance, from 628 nm back to 541 nm, Figure 4C. The fitted interparticle distance also dramatically increases from the close-packed 10 nm to sparsely distributed 45 nm, meaning the majority of the NPs have left the SLI.

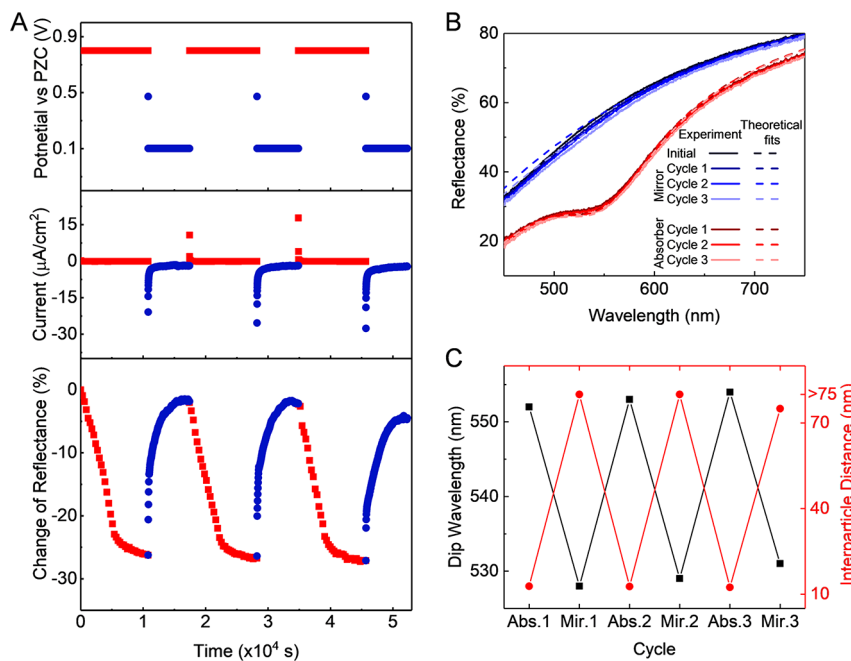


Figure 6. Reversible switching of the system between the “mirror” state (0.1 V vs PZC) and the “absorber” state (0.7 V vs PZC). (A) Electrode potential over time (top), the corresponding electrochemical current (middle), and the change of reflection dip (bottom). (B) The “mirror” and “absorber” spectra at different cycles. (C) Dip wavelength and interparticle distance for the “absorber” (Abs.) and “mirror” (Mir.) states at different cycles.

By subtracting the reflectance of pristine TiN/Ag, Figure 4D shows how the dip diminishes when the electrode potential is decreased and the system gets back to the “mirror” state. A more quantitative look at the dip position shows a reversed trend when compared with the assembly process: the loss of reflectance recovers from -30% to almost zero and the dip wavelength also shifts from 556 nm back to 528 nm, Figure 4E.

Similar to the assembly process, we monitored the dynamics of the disassembly process by implementing a jump-wise change in the electrode potential from 0.7 to 0.1 V versus PZC. The closely matched experimental data and theoretical fits depict how the densely packed NP array on the substrate becomes more reflective and can revert back to its “mirror” state, Figure 5A,B. This is quantified in Figure 5C, where the wavelength of the dip blue-shifts back from 555 to 528 nm and the depth of the dip decreases from -30% to almost 0. Values of the coverage θ , estimated by EMT-fitting, give us a picture of the kinetics of disassembly. The time dependence of the coverage during disassembly follows a simple model. One can assume that very low, negative potentials make the energy barrier much lower for desorption, compared to adsorption. This allows us to neglect the adsorption rate in the kinetic Langmuir adsorption isotherm resulting in a trivial, exponential decay of the coverage. Confirmation of such law is shown in Figure 5D.

Having demonstrated the “mirror” state (after the NPs leave the interface) and an “absorber” state (after the NPs assemble at the interface), we check reversibility of this process in the same system. Figure 6A shows the switching between these two states over multiple cycles. We start by polarizing the electrode at 0.7 V versus PZC. While such a value is maintained (“red-labeled” regions), the reflectance slowly drops down, meaning that NPs are assembling onto the substrate. Switching the potential to 0.1 V (“blue” regions) leads to the increase in reflectance, bringing the system back to

the “mirror” state. The spectra of “mirror” and “absorber” states in these cycles are shown in Figure 6B alongside with the dip wavelength and interparticle distance (Figure 6C), demonstrating the system can be switched on and off for multiple times. No NP aggregation is witnessed in the bulk solution after reversibility experiments (Figure S4).

A closer examination of the spectra reveals a tiny dip for the mirror state after multiple cycles. Theoretical fitting also gives an interparticle spacing of 75 nm for the final cycle. This means that after the disassembly process, a small number of NPs are still “stuck” at the SLI. As has been mentioned previously, there is an energy barrier for adsorption in the vicinity of the SLI. If the negative potential is not large enough for totally removing this barrier, some NPs could still be (at least kinetically) trapped. To totally remove those NPs for fully recovery, a substantial negative potential is needed. This will require the use of nonaqueous solutions that will allow higher electrode potentials.

CONCLUSIONS

We have demonstrated electrotunable reflectivity of light from a solid electrode in electrolytic solutions, the spectra of which get modified by voltage-controlled physisorption of plasmonic NPs.

A positively polarized planar TiN/Ag-electrode attracts negatively charged 16 nm AuNPs leading to formation of adsorbed two-dimensional arrays of NPs. Making potential more negative repels NPs from the electrodes, disassembling the array. For this system, the coupling of surface plasmon modes in the electrode with localized coupled plasmon resonances in the adsorbed NPs leads to the suppressed reflection in green, making the substrates red colored. But after NPs leave the interface, its optical response returns to the one of the bare TiN/Ag-electrode. The switching between these two states is reversible.

Table 1. Drude-Lorentz (DL) Fitting Parameters for Bulk Au, TiN, and Ag

	ϵ_∞	ω_p (eV)	γ_p (eV)	f_1	ω_1 (eV)	γ_1 (eV)	f_2	ω_2 (eV)	γ_2 (eV)
Au	5.0896	9.0271	0.0760	1.4288	2.9530	0.9541	1.8465	4.0616	1.5639
TiN	1.1667	4.9652	3.0574	2.4881	12.877	22.407	4.8438	5.8305	5.2834
Ag	3.7180	9.2093	0.0200	0.4242	4.2840	0.3430			

By adjusting the electric potential of the Ag substrate or the NaCl concentration of NP solution, the interparticle distance of this NP array at the SLI could be finely tuned, allowing control of both the wavelength and intensity of the reflectance dip.

The EMT theory of the optical response of this system relates the optical properties of the interface with adsorbed NPs to optical polarizability of NPs and the structure of the adsorbed NP arrays. Fitting the theory to the reflectivity data allows for the extraction of the average distance between NPs in the arrays, both at equilibrium and during assembly/disassembly.

Extracting the time-dependent coverage of the electrode by NPs from the evolution of reflectance spectrum, and subsequent treatment of the results with the kinetic theory of adsorption–desorption, suggest that (i) both the adsorption and the desorption stages have to overcome energy barriers that are affected by electrode potential; (ii) the account of all three stages—diffusion, adsorption, and desorption—is important for interpreting the data, except for disassembly at low potentials which follows a much simpler law.

The observed rates of assembly/disassembly in the convection-free system are too slow for practical applications where fast-switching is required. Had those kinetics been exclusively diffusion limited, the natural solution to the problem would have been miniaturization of the cell⁷⁰ to shorten the diffusion path. However, that only partially solves the problem.

Indeed, the seemingly present free energy barriers for adsorption and desorption point at the necessity of creating a system with a larger electrochemical window, so that higher electrode potentials (greater than 1 V) could be applied to lower or fully eliminate those barriers.

The presented work demonstrates a proof of concept for a new type of electrovariable plasmonic reflector. Converting this to a practical, tunable optical device will be the subject of future investigations, along the way paved in this work.

METHODS

MDA Capped Gold Nanoparticles. A 500 mL aliquot of 0.01 wt % HAuCl₄ solution was heated to boil on a hot plate with magnetic stirring. Then 10 mL of 1 wt % sodium citrate was quickly pipetted into the boiling solution which was kept for 30 min to allow the reaction to finish. The resultant red NP solution was then cooled to 60 °C and 3 mg MDA was added. After maintaining the temperature for 2 h, the NP solution was allowed to naturally cool to room temperature and stored in a fridge for further use. The designated pH was reached by adding certain volume of 100 mM NaOH with the monitoring from a pH meter (SevenGo Duo pro, Mettler Toledo). We checked the concentration and the dispersity of NPs by a UV-vis spectrometer (Nanodrop 2000, Thermo Scientific), the diameter of NPs (Figure S1A,B) by transmission electron microscope (TEM, JEOL 2100 PLUS) and the presence of NPs on substrates by scanning electron microscope (SEM, LEO Gemini 1525 FEGSEM).

For SEM sample preparation, the NPs were deposited on to the TiN/Ag substrate overnight and was carefully removed from the NP solution and quickly dried using a nitrogen gas line. No further coating was applied before the SEM imaging.

TiN/Ag Substrates. Silicon substrates were first stripped of their native oxide layer in a hydrofluoric acid bath. A 2 nm Ti adhesion layer was then evaporated onto the substrate, followed by a 125 nm Ag layer. The sample was then immediately placed in a plasma-enhanced atomic layer deposition (PEALD) system, where 10 nm of TiN was deposited at a temperature of 270 °C. The sample was left to cool in the chamber before exposing it to atmosphere in order to avoid excessive oxidation. Before use, the TiN/Ag substrates were intensively rinsed by acetone, ethanol, and DI water.

Electrochemical-Optical Setup and Measurements. As shown in Figure 1A(ii), a TiN/Ag substrate was inserted into a polytetrafluoroethylene (PTFE) holder, which connects the substrate with a platinum wire leading to the working electrode. Two other holes on the holder were used to accommodate a Ag/AgCl reference electrode and platinum counter electrode, respectively. An Ocean Optics reflection probe with a focal length of 2 mm was placed above the substrate with normal orientation. The white light emitted by a tungsten halogen lamp (Ocean Optics) was transmitted through a multimode fiber onto the same. The collected light was focused on to an Andor 163 spectrograph fitted with an iDus charge-coupled device. A Thorlabs silver mirror was used as an optical reference. The Gamry potentiostat applied potential to the substrate while the synchronized Andor spectrometer collected the reflected signals from the substrate simultaneously. The absorbance from the bulk solution between the optical probe and the substrate are subtracted in all data sets.

Theory of Reflection Spectra. A five-layer stack model⁵⁵ was adopted to calculate the optical reflectance spectra, for which the first step is to accurately determine the permittivity of each layer. In doing so, we considered the NP surrounding medium [layers 1 and 3 (refer to Figure S5)] to be frequency-independent ($\epsilon_1 \equiv \epsilon_3$). On the other hand, the Au NP layer (layer 2) and the substrate layers (layers 4 and 5) were characterized by frequency-dependent dielectric constants, which were modeled by a Drude-Lorentz (DL) formula with parameters listed in Table 1:

$$\epsilon(\omega) = \epsilon_\infty - \frac{\omega_p^2}{\omega^2 + i\gamma_p^2\omega} - f_1 \frac{\omega_1^2}{\omega^2 - \omega_1^2 - i\gamma_1^2\omega} - f_2 \frac{\omega_2^2}{\omega^2 - \omega_2^2 - i\gamma_2^2\omega} \quad (1)$$

For 8 nm radius Au NPs considered in this work, it is important to account for their finite size effects by considering for surface electron scattering in the DL model. Generally, for Au NPs smaller than the electron mean free path (~42 nm for Au), the plasma damping coefficient⁷¹ gets a correction that for spherical particles reads:

$$\gamma_p = \gamma_p^{(0)} + A \frac{v_F}{R}, \quad (2)$$

where $\gamma_p^{(0)}$ is the plasma damping factor of the bulk Au material as in the table above, $A \approx 0.25$ is a constant determined experimentally, v_F is Fermi velocity of electrons in gold, and R is the particle radius: for 8 nm radius gold NPs, this correction gives $\gamma_p = 0.25017$ eV. This size-dependent Au permittivity was then used for obtaining the permittivity of the NP layer (layer 2) using the equations described in the [SI, section 4](#).

In using the five-layer stack model, the critical step is to describe the optical properties of the NP layer using our EMT approach, which estimates the effective quasi-static polarizability of individual NPs in the presence of other NPs arranged in a two-dimensional, hexagonal lattice.⁵³ Then multilayer Fresnel reflection theory is used with our effective medium theory approach to obtain the reflectance spectra of the system under study. Refer to the [SI, section 4](#) for details.

For wavelengths below 500 nm, the contributions from higher-order modes, possessing higher energy than dipolar mode, become more prominent. This effect is not considered in our EMT, which is developed based on quasi-static dipolar approximations.

Note that, at LLIs in nonelectrochemical configurations, the structure of the NP arrays and their dependence of the concentrations of electrolytes, was characterized by synchrotron X-ray diffraction.³⁴ Having determined the distances between NPs from X-ray diffraction data, theoretical optical reflection spectra were calculated using EMT.²³ In parallel, the experimental reflectance spectra were obtained there as well, showing excellent match between theory and experiments. Similar X-ray characterization of NP arrays at electrochemical SLI will require much more complicated cell design, and it has not yet been performed. However, excellent correspondence between the measured and calculated spectra shown in the present paper proves that one can use the reflectance spectra to assess the distances between the NP in adsorbed arrays.

Theory of Assembly Kinetics. The kinetics of assembly of particles at the interface is generally determined by three rates, of adsorption, desorption, and diffusion. The account of all three contributions to this process, following Miura and Seki,⁶⁹ leads to an integro-differential equation on fractional coverage, θ :

$$\frac{d\theta}{d\tau} = \left[r - \int_0^\tau \frac{1}{\sqrt{\pi(\tau - \tau_1)}} \frac{d\theta}{d\tau_1} d\tau_1 \right] (1 - \theta) - \kappa_d \theta \quad (3)$$

The above equation establishes the coverage dependence on dimensionless time, τ , and parameters r and κ_d . All these dimensionless quantities can be expressed, in terms of adsorption and desorption constants (k_a , k_d), diffusion coefficient (D), maximum coverage (Γ_m), bulk concentration (c_0), and time (t) as follows:

$$\tau = \frac{k_a^2 \Gamma_m^2}{D} t, \quad r = \frac{D c_0}{k_a \Gamma_m^2}, \quad \kappa_d = \frac{D}{k_a^2 \Gamma_m^2} k_d \quad (4)$$

Note that this equation does not take into account interactions between the adsorbed particles except for the limitation on the number of available sites for them. Nevertheless, we were able to use it because at the values of interparticle separations that reflectance experiments established (≈ 10 nm NP surface-to-surface separation) interactions

between particles are heavily screened by electrolyte (Debye length, $L_D = 1.24$ nm). The solution to this equation, when all three rates are comparable, can only be obtained numerically, but there are two limiting cases when analytical solutions are possible.

The first one is the adsorption–desorption controlled regime, when diffusion limitations are insignificant. Under such conditions, the integral in [eq 3](#) becomes small compared to parameters r and κ_d and can, therefore, be neglected. This simplification allows for an easy separation of variables, followed by integration, giving

$$\theta = \frac{r}{r + \kappa_d} [1 - e^{-(r + \kappa_d)\tau}] \quad (5)$$

The main assumption behind this limiting case is valid whenever particles have to overcome a high free energy barrier (both into and out of the adsorption well), as adsorption and desorption will become very slow compared to diffusion. The second case occurs when diffusion is rate determining, and is modeled by the following equation, which partially takes saturation into account:

$$\theta = 1 - e^{-2c_0/\Gamma_m \sqrt{\frac{Dt}{\pi}}} \quad (6)$$

Fitting our adsorption kinetics data to either [eq 5](#) or [eq 6](#) does not show a good match, and hence, we need to implement the full [eq 3](#).

Electrostatic Interactions (between Two Adjacent Particles) near a Solid–Liquid Interface. The derivation of the equations below are presented in ref [72](#), so here we will just give a brief summary of them and the physics behind them. From an electrostatic viewpoint, the two phases (electrolyte-I and electrode-II) are characterized by their dielectric properties and ability to screen electric fields. While dielectric properties are quantified by their respective dielectric constants, ϵ_I and ϵ_{II} , the electrostatic screening properties can be described by characteristic screening lengths, k_I^{-1} and k_{II}^{-1} . In this case, k_I^{-1} is the Debye screening length of the electrolyte, a measure of how efficient ions can rearrange in order to screen electric field. Similarly, k_{II}^{-1} is the so-called Thomas-Fermi length, describing the distance of electric field penetration into the electrode. Based on the linear Poisson–Boltzmann equation, both pair and image interactions can be derived.

[Equation 7](#) shows the result of the pair interaction near the electrode.

$$\frac{W}{kT} = N^2 L_B \left(\frac{\sinh(k_I R)}{k_I R} \right)^2 \times \left(\frac{e^{-k_I R_0}}{R_0} \right) + \int_0^\infty \frac{K dK}{\sqrt{k^2 + k_I^2}} \frac{\epsilon_I \sqrt{k^2 + k_I^2} - \epsilon_{II} \sqrt{k^2 + k_{II}^2}}{\epsilon_I \sqrt{k^2 + k_I^2} + \epsilon_{II} \sqrt{k^2 + k_{II}^2}} \times e^{-2\sqrt{k^2 + k_I^2} z_0} J_0(K R_0) \quad (7)$$

Here, N is the number of elementary charges per NP, L_B is the Bjerrum Length, R is the particle radius, z_0 is the distance of the center of the NP from the interface, R_0 is the center-to-center distance between the particles, and K is the variable of integration. While the sinh factor, which depends on the NP radius, accounts for the curvature contribution, the last factor incorporates two terms. The first one is the well-known Yukawa potential, which expresses the direct interaction between the particles in the bulk. The second term is a correction, which models the interaction between one of the two particles and the image of the other. The predictions given by this equation are shown in [Figure S3](#), confirming that it is

preferable to choose the highest concentration, which does not destabilize the bulk solution.

The interaction between each particle and the electrode can also be modeled in a similar manner, based on two separate contributions. The first one, from image forces, is given by the following expression, which is also based on the linear Poisson–Boltzmann equation:

$$\frac{W}{kT} = N^2 \frac{L_B}{2} \left(\frac{\sinh(k_l R)}{k_l R} \right)^2 \times \int_0^\infty \frac{K dK}{\sqrt{K^2 + k_l^2}} \frac{\epsilon_{1I} \sqrt{K^2 + k_l^2} - \epsilon_{II} \sqrt{K^2 + k_l^2}}{\epsilon_{1I} \sqrt{K^2 + k_l^2} + \epsilon_{II} \sqrt{K^2 + k_l^2}} e^{-2\sqrt{K^2 + k_l^2} z_0} \quad (8)$$

The second contribution comes from the interaction with the free charge on the electrode, which is present whenever the potential deviates from the PZC. eq 9 is a simple estimate of that contribution which, nevertheless, takes into account the nonlinear screening of electrode potentials:

$$\frac{W}{kT} = \frac{2N}{R} \int_0^a \ln \frac{\coth\left(\frac{eV_0}{4kT}\right) + e^{-k_l(z_0-t)}}{\coth\left(\frac{eV_0}{4kT}\right) - e^{-k_l(z_0-t)}} dt \quad (9)$$

where V_0 is the electrode potential vs PZC and e is the elementary charge.

These equations describe only electrostatic interactions between NPs and the interface and between each other. They are used to plot the curves in Figure 1D. In ref 72, the detailed analysis of the contribution of the corresponding van der Waals interactions is also performed, and they are found to give a smaller contribution. The analysis of the effects of electronic polarizability of NPs⁷³ were not performed, but those are believed to be much smaller than direct and image interactions for particles that are highly charged by MDDA ligands.

ASSOCIATED CONTENT

Supporting Information

The Supporting Information is available free of charge on the ACS Publications website at DOI: [10.1021/acsphtnics.8b01105](https://doi.org/10.1021/acsphtnics.8b01105).

The detailed information about NPs, brief review of five-layer stack model for reflection spectra, analysis of the effect of dispersion of interparticle distances, analysis of dried samples, calculation of the coverage, and additional analysis of the NPs' kinetic adsorption isotherm ([PDF](#)).

AUTHOR INFORMATION

Corresponding Authors

*E-mail: a.kucernak@imperial.ac.uk.

*E-mail: joshua.edel@imperial.ac.uk.

*E-mail: a.kornyshev@imperial.ac.uk.

ORCID

Sang-Hyun Oh: [0000-0002-6992-5007](https://orcid.org/0000-0002-6992-5007)

Anthony R. Kucernak: [0000-0002-5790-9683](https://orcid.org/0000-0002-5790-9683)

Joshua B. Edel: [0000-0001-5870-8659](https://orcid.org/0000-0001-5870-8659)

Alexei A. Kornyshev: [0000-0002-3157-8791](https://orcid.org/0000-0002-3157-8791)

Notes

The authors declare no competing financial interest.

ACKNOWLEDGMENTS

The project was supported by an Engineering and Physical Sciences Research Council Grant, “Electrotunable Molecular Alarm”, EP/L02098X/1. J.B.E. also acknowledges receipt of European Research Council Consolidator Grant (NanoPD). Y.M. has been supported in part by a China Scholarship Council, Imperial Scholarship (201506320194). D.J.K. and S.-H.O. acknowledge support from Seagate Technology through the Centre for Micromagnetics and Information Technologies (MINT) at the University of Minnesota. D.S. also acknowledges the support of a H2020-MSCA individual fellowship. Discussions and previous work with Prof. Michael Urbakh (TAU) are gratefully acknowledged.

REFERENCES

- Zheludev, N. I.; Kivshar, Y. S. From Metamaterials to Metadevices. *Nat. Mater.* **2012**, *11*, 917–924.
- Cai, W.; Shalaev, V. *Optical Metamaterials: Fundamentals and Applications*; Cai, W., Shalaev, V., Eds.; Springer: New York, 2016; pp 1–10.
- Schuller, J. A.; Barnard, E. S.; Cai, W.; Jun, Y. C.; White, J. S.; Brongersma, M. L. Plasmonics for Extreme Light Concentration and Manipulation. *Nat. Mater.* **2010**, *9*, 193–204.
- Lal, S.; Link, S.; Halas, N. J. Nano-Optics from Sensing to Waveguiding. *Nat. Photonics* **2007**, *1*, 641–648.
- Wang, W.; Ramezani, M.; Väkeväinen, A. I.; Törmä, P.; Rivas, J. G.; Odom, T. W. The rich photonic world of plasmonic nanoparticle arrays. *Mater. Today* **2018**, *21*, 303–314.
- Chen, H. S.; Zheng, B.; Shen, L.; Wang, H. P.; Zhang, X. M.; Zheludev, N. I.; Zhang, B. L. Ray-Optics Cloaking Devices for Large Objects in Incoherent Natural Light. *Nat. Commun.* **2013**, *4*, 2652.
- Pendry, J. B.; Schurig, D.; Smith, D. R. Controlling Electromagnetic Fields. *Science* **2006**, *312*, 1780–1782.
- Lu, D. L.; Liu, Z. W. Hyperlenses and Metolenses for Far-Field Super-Resolution Imaging. *Nat. Commun.* **2012**, *3*, 1205.
- Wang, Q.; Rogers, E. T. F.; Gholipour, B.; Wang, C. M.; Yuan, G. H.; Teng, J. H.; Zheludev, N. I. Optically Reconfigurable Metasurfaces and Photonic Devices Based on Phase Change Materials. *Nat. Photonics* **2016**, *10*, 60–65.
- Pendry, J. B.; Luo, Y.; Zhao, R. K. Transforming the Optical Landscape. *Science* **2015**, *348*, 521–524.
- Xiong, K.; Tordera, D.; Emilsson, G.; Olsson, O.; Linderhed, U.; Jonsson, M. P.; Dahlin, A. B. Switchable Plasmonic Metasurfaces with High Chromaticity Containing Only Abundant Metals. *Nano Lett.* **2017**, *17*, 7033–7039.
- Kunli, X.; Gustav, E.; Ali, M.; Xinjin, Y.; Lei, S.; H, J. E. W.; B, D. A. Plasmonic Metasurfaces with Conjugated Polymers for Flexible Electronic Paper in Color. *Adv. Mater.* **2016**, *28*, 9956–9960.
- Li, W.; Valentine, J. Metamaterial Perfect Absorber Based Hot Electron Photodetection. *Nano Lett.* **2014**, *14*, 3510–3514.
- Atwater, H. A.; Polman, A. Plasmonics for Improved Photovoltaic Devices. *Nat. Mater.* **2010**, *9*, 205–213.
- Tordera, D.; Zhao, D.; Volkov, A. V.; Crispin, X.; Jonsson, M. P. Thermoplasmonic Semitransparent Nanohole Electrodes. *Nano Lett.* **2017**, *17*, 3145–3151.
- Jonsson, G.; Tordera, D.; Pakizeh, T.; Jaysankar, M.; Miljkovic, V.; Tong, L. M.; Jonsson, M. P.; Dmitriev, A. Solar Transparent Radiators by Optical Nanoantennas. *Nano Lett.* **2017**, *17*, 6766–6772.
- Zheludev, N. I. The Road Ahead for Metamaterials. *Science* **2010**, *328*, 582–583.
- Fan, Z.; Govorov, A. O. Plasmonic Circular Dichroism of Chiral Metal Nanoparticle Assemblies. *Nano Lett.* **2010**, *10*, 2580–2587.
- Yang, A.; Hryn, A. J.; Bourgeois, M. R.; Lee, W.-K.; Hu, J.; Schatz, G. C.; Odom, T. W. Programmable and reversible plasmon mode engineering. *Proc. Natl. Acad. Sci. U. S. A.* **2016**, *113*, 14201–14206.

- (20) Maier, S. A. *Plasmonics: Fundamentals and Applications*; Maier, S. A., Ed.; Springer: New York, 2007; pp 65–88.
- (21) Halas, N. J.; Lal, S.; Chang, W. S.; Link, S.; Nordlander, P. Plasmons in Strongly Coupled Metallic Nanostructures. *Chem. Rev.* **2011**, *111*, 3913–3961.
- (22) Wang, D.; Yang, A.; Hryny, A. J.; Schatz, G. C.; Odom, T. W. Superlattice Plasmons in Hierarchical Au Nanoparticle Arrays. *ACS Photonics* **2015**, *2*, 1789–1794.
- (23) Litt, D. B.; Jones, M. R.; Hentschel, M.; Wang, Y.; Yang, S.; Ha, H. D.; Zhang, X.; Alivisatos, A. P. Hybrid Lithographic and DNA-Directed Assembly of a Configurable Plasmonic Metamaterial That Exhibits Electromagnetically Induced Transparency. *Nano Lett.* **2018**, *18*, 859–864.
- (24) Ou, J. Y.; Plum, E.; Zhang, J. F.; Zheludev, N. I. An Electromechanically Reconfigurable Plasmonic Metamaterial Operating in the Near-Infrared. *Nat. Nanotechnol.* **2013**, *8*, 252–255.
- (25) Shin, D.; Urzhumov, Y.; Jung, Y.; Kang, G.; Baek, S.; Choi, M.; Park, H.; Kim, K.; Smith, D. R. Broadband Electromagnetic Cloaking with Smart Metamaterials. *Nat. Commun.* **2012**, *3*, 1213.
- (26) Si, K. J.; Sikdar, D.; Chen, Y.; Eftekhari, F.; Xu, Z.; Tang, Y.; Xiong, W.; Guo, P.; Zhang, S.; Lu, Y.; et al. Giant Plasmene Nanosheets, Nanoribbons, and Origami. *ACS Nano* **2014**, *8*, 11086–11093.
- (27) Ou, J. Y.; Plum, E.; Jiang, L.; Zheludev, N. I. Reconfigurable Photonic Metamaterials. *Nano Lett.* **2011**, *11*, 2142–2144.
- (28) Shevchenko, E. V.; Talapin, D. V.; Kotov, N. A.; O'Brien, S.; Murray, C. B. Structural Diversity in Binary Nanoparticle Superlattices. *Nature* **2006**, *439*, 55–59.
- (29) Edel, J. B.; Kornyshev, A. A.; Kucernak, A. R.; Urbakh, M. Fundamentals and Applications of Self-Assembled Plasmonic Nanoparticles at Interfaces. *Chem. Soc. Rev.* **2016**, *45*, 1581–1596.
- (30) Scanlon, M. D.; Smirnov, E.; Stockmann, T. J.; Peljo, P. Gold Nanofilms at Liquid–Liquid Interfaces: An Emerging Platform for Redox Electrocatalysis, Nanoplasmonic Sensors, and Electrovariable Optics. *Chem. Rev.* **2018**, *118*, 3722–3751.
- (31) Bera, M. K.; Chan, H.; Moyano, D. F.; Yu, H.; Tatur, S.; Amoanu, D.; Bu, W.; Rotello, V. M.; Meron, M.; Král, P.; et al. Interfacial Localization and Voltage-Tunable Arrays of Charged Nanoparticles. *Nano Lett.* **2014**, *14*, 6816–6822.
- (32) Edel, J. B.; Kornyshev, A. A.; Urbakh, M. Self-Assembly of Nanoparticle Arrays for Use as Mirrors, Sensors, and Antennas. *ACS Nano* **2013**, *7*, 9526–9532.
- (33) Booth, S. G.; Dryfe, R. A. W. Assembly of Nanoscale Objects at the Liquid/Liquid Interface. *J. Phys. Chem. C* **2015**, *119*, 23295–23309.
- (34) Su, B.; Abid, J.-P.; Fermín, D. J.; Girault, H. H.; Hoffmannová, H.; Krtík, P.; Samec, Z. Reversible Voltage-Induced Assembly of Au Nanoparticles at Liquid/Liquid Interfaces. *J. Am. Chem. Soc.* **2004**, *126*, 915–919.
- (35) Velleman, L.; Sikdar, D.; Turek, V. A.; Kucernak, A. R.; Roser, S. J.; Kornyshev, A. A.; Edel, J. B. Tuneable 2d Self-Assembly of Plasmonic Nanoparticles at Liquid/Liquid Interfaces. *Nanoscale* **2016**, *8*, 19229–19241.
- (36) Kiely, C. J.; Fink, J.; Brust, M.; Bethell, D.; Schiffrin, D. J. Spontaneous Ordering of Bimodal Ensembles of Nanoscopic Gold Clusters. *Nature* **1998**, *396*, 444–446.
- (37) Smirnov, E.; Peljo, P.; Scanlon, M. D.; Gumy, F.; Girault, H. H. Self-Healing Gold Mirrors and Filters at Liquid-Liquid Interfaces. *Nanoscale* **2016**, *8*, 7723–7737.
- (38) Hentschel, M.; Saliba, M.; Vogelgesang, R.; Giessen, H.; Alivisatos, A. P.; Liu, N. Transition from Isolated to Collective Modes in Plasmonic Oligomers. *Nano Lett.* **2010**, *10*, 2721–2726.
- (39) Kim, J.-W.; Kovalenko, O.; Liu, Y.; Bigot, J.-Y. Exploring the Angstrom Excursion of Au Nanoparticles Excited away from a Metal Surface by an Impulsive Acoustic Perturbation. *ACS Nano* **2016**, *10*, 10880–10886.
- (40) Lalander, C. H.; Zheng, Y.; Dhuey, S.; Cabrini, S.; Bach, U. DNA-Directed Self-Assembly of Gold Nanoparticles onto Nano-patterned Surfaces: Controlled Placement of Individual Nanoparticles into Regular Arrays. *ACS Nano* **2010**, *4*, 6153–6161.
- (41) Lassiter, J. B.; McGuire, F.; Mock, J. J.; Ciraci, C.; Hill, R. T.; Wiley, B. J.; Chilkoti, A.; Smith, D. R. Plasmonic Waveguide Modes of Film-Coupled Metallic Nanocubes. *Nano Lett.* **2013**, *13*, 5866–5872.
- (42) Ciraci, C.; Chen, X.; Mock, J. J.; McGuire, F.; Liu, X.; Oh, S.-H.; Smith, D. R. Film-Coupled Nanoparticles by Atomic Layer Deposition: Comparison with Organic Spacing Layers. *Appl. Phys. Lett.* **2014**, *104*, 023109.
- (43) Cao, S.-H.; Cai, W.-P.; Liu, Q.; Xie, K.-X.; Weng, Y.-H.; Huo, S.-X.; Tian, Z.-Q.; Li, Y.-Q. Label-Free Aptasensor Based on Ultrathin-Linker-Mediated Hot-Spot Assembly To Induce Strong Directional Fluorescence. *J. Am. Chem. Soc.* **2014**, *136*, 6802–6805.
- (44) Yavas, O.; Svedendahl, M.; Dobosz, P.; Sanz, V.; Quidant, R. On-a-chip Biosensing Based on All-Dielectric Nanoresonators. *Nano Lett.* **2017**, *17*, 4421–4426.
- (45) Hu, M.; Ghoshal, A.; Marquez, M.; Kik, P. G. Single Particle Spectroscopy Study of Metal-Film-Induced Tuning of Silver Nanoparticle Plasmon Resonances. *J. Phys. Chem. C* **2010**, *114*, 7509–7514.
- (46) Li, C.-Y.; Gao, J.-H.; Yi, J.; Zhang, X.-G.; Cao, X.-D.; Meng, M.; Wang, C.; Huang, Y.-P.; Zhang, S.-J.; Wu, D.-Y.; et al. Plasmon-Enhanced Ultrasensitive Surface Analysis Using Ag Nanoantenna. *Anal. Chem.* **2018**, *90*, 2018–2022.
- (47) Lacharmoise, P. D.; Le Ru, E. C.; Etchegoin, P. G. Guiding Molecules with Electrostatic Forces in Surface Enhanced Raman Spectroscopy. *ACS Nano* **2009**, *3*, 66–72.
- (48) Lumdee, C.; Toroghi, S.; Kik, P. G. Post-fabrication Voltage Controlled Resonance Tuning of Nanoscale Plasmonic Antennas. *ACS Nano* **2012**, *6*, 6301–6307.
- (49) Park, C.; Seo, S.; Shin, H.; Sarwade, B. D.; Na, J.; Kim, E. Switchable Silver Mirrors with Long Memory Effects. *Chem. Sci.* **2015**, *6*, 596–602.
- (50) Ding, T.; Sigle, D.; Zhang, L.; Mertens, J.; de Nijs, B.; Baumberg, J. Controllable Tuning Plasmonic Coupling with Nano-scale Oxidation. *ACS Nano* **2015**, *9*, 6110–6118.
- (51) Sikdar, D.; Bucher, A.; Zagar, C.; Kornyshev, A. A. Electrochemical Plasmonic Metamaterials: Towards Fast Electro-Tunable Reflecting Nanoshutters. *Faraday Discuss.* **2017**, *199*, 585–602.
- (52) Mock, J. J.; Hill, R. T.; Tsai, Y.-J.; Chilkoti, A.; Smith, D. R. Probing Dynamically Tunable Localized Surface Plasmon Resonances of Film-Coupled Nanoparticles by Evanescent Wave Excitation. *Nano Lett.* **2012**, *12*, 1757–1764.
- (53) Di Martino, G.; Turek, V. A.; Lombardi, A.; Szabó, I.; de Nijs, B.; Kuhn, A.; Rosta, E.; Baumberg, J. J. Tracking Nanoelectrochemistry Using Individual Plasmonic Nanocavities. *Nano Lett.* **2017**, *17*, 4840–4845.
- (54) Montelongo, Y.; Sikdar, D.; Ma, Y.; McIntosh, A. J. S.; Velleman, L.; Kucernak, A. R.; Edel, J. B.; Kornyshev, A. A. Electrotunable Nanoplasmonic Liquid Mirror. *Nat. Mater.* **2017**, *16*, 1127–1135.
- (55) Sikdar, D.; Hasan, S. B.; Urbakh, M.; Edel, J. B.; Kornyshev, A. A. Unravelling the Optical Responses of Nanoplasmonic Mirror-on-Mirror Metamaterials. *Phys. Chem. Chem. Phys.* **2016**, *18*, 20486–20498.
- (56) Sikdar, D.; Kornyshev, A. A. Theory of Tailorable Optical Response of Two-Dimensional Arrays of Plasmonic Nanoparticles at Dielectric Interfaces. *Sci. Rep.* **2016**, *6*, 33712.
- (57) Solovan, M. N.; Brus, V. V.; Maistruk, E. V.; Maryanchuk, P. D. Electrical and Optical Properties of Tin Thin Films. *Inorg. Mater.* **2014**, *50*, 40–45.
- (58) Dimitriadis, C. A.; Logothetidis, S.; Alexandrou, I. Schottky-Barrier Contacts of Titanium Nitride on N-Type Silicon. *Appl. Phys. Lett.* **1995**, *66*, 502–504.
- (59) Naik, G. V.; Shalaev, V. M.; Boltasseva, A. Alternative Plasmonic Materials: Beyond Gold and Silver. *Adv. Mater.* **2013**, *25*, 3264–3294.

- (60) He, D.; Bligh, M. W.; Waite, T. D. Effects of Aggregate Structure on the Dissolution Kinetics of Citrate-Stabilized Silver Nanoparticles. *Environ. Sci. Technol.* **2013**, *47*, 9148–9156.
- (61) Borzenkov, M.; Chirico, G.; D’Alfonso, L.; Sironi, L.; Collini, M.; Cabrini, E.; Dacarro, G.; Milanese, C.; Pallavicini, P.; Taglietti, A.; et al. Thermal and Chemical Stability of Thiol Bonding on Gold Nanostars. *Langmuir* **2015**, *31*, 8081–8091.
- (62) Massiani, Y.; Medjahed, A.; Picq, G. Photoelectrochemical Characterization of Oxidized Films of Titanium Nitride and Titanium Obtained by Reaction Sputtering. *Thin Solid Films* **1992**, *207*, 109–116.
- (63) Gelderman, K.; Lee, L.; Donne, S. W. Flat-Band Potential of a Semiconductor: Using the Mott–Schottky Equation. *J. Chem. Educ.* **2007**, *84*, 685–688.
- (64) Grahame, D. C. The Electrical Double Layer and the Theory of Electrocapillarity. *Chem. Rev.* **1947**, *41*, 441–501.
- (65) Morrison, S. R. *Electrochemistry at Semiconductor and Oxidized Metal Electrodes*; Morrison, S. R., Ed.; Springer: New York, 2011; pp 119–149.
- (66) Li, C.-T.; Li, S.-R.; Chang, L.-Y.; Lee, C.-P.; Chen, P.-Y.; Sun, S.-S.; Lin, J.-J.; Vittal, R.; Ho, K.-C. Efficient Titanium Nitride/Titanium Oxide Composite Photoanodes for Dye-Sensitized Solar Cells and Water Splitting. *J. Mater. Chem. A* **2015**, *3*, 4695–4705.
- (67) McShane, C. M.; Choi, K.-S. Photocurrent Enhancement of n-Type Cu₂O Electrodes Achieved by Controlling Dendritic Branching Growth. *J. Am. Chem. Soc.* **2009**, *131*, 2561–2569.
- (68) Turek, V. A.; Cecchini, M. P.; Paget, J.; Kucernak, A. R.; Kornyshev, A. A.; Edel, J. B. Plasmonic Ruler at the Liquid–Liquid Interface. *ACS Nano* **2012**, *6*, 7789–7799.
- (69) Miura, T.; Seki, K. Diffusion Influenced Adsorption Kinetics. *J. Phys. Chem. B* **2015**, *119*, 10954–10961.
- (70) Kang, S.; Mathwig, K.; Lemay, S. G. Response Time of Nanofluidic Electrochemical Sensors. *Lab Chip* **2012**, *12*, 1262–1267.
- (71) Berciaud, S.; Cognet, L.; Tamarat, P.; Lounis, B. Observation of Intrinsic Size Effects in the Optical Response of Individual Gold Nanoparticles. *Nano Lett.* **2005**, *5*, 515–518.
- (72) Zagar, Z.; Rhys-Griffiths, R.; Podgornik, R.; Kornyshev, A. A. On the Voltage-Controlled Assembly of NP Arrays at Electrochemical Solid/Liquid Interfaces. *arXiv:1810.05019, arXiv.org e-Print archive* **2018**, na.
- (73) Peljo, P.; Manzanares, J. A.; Girault, H. H. Contact Potentials, Fermi Level Equilibration, and Surface Charging. *Langmuir* **2016**, *32*, 5765–5775.